Detection, quantification and characterisation by digital image analysis method of bacterial infection by _Vibrio aestuarianus_, stained by immunohistochemistry, in the pacific oyster _Magallana gigas_

1
2
3

Valentin Geslin[1*], Leila Parizadeh[2], Marie-Agnès Travers[3], Luca Tomasetti[4], Thor Ole

Gulsrud[5]

[1] University of Stavanger, Faculty of Science and Technology, Department of

Chemistry, Bioscience and Environmental Engineering, Norway

[2] La Rochelle Université, Laboratoire LIttoral ENvironnement et Sociétés (LIENSs),

UMR 7266, CNRS - La Rochelle, France

[3] IHPE, Univ Montpellier, CNRS, IFREMER, Univ Perpignan Via Domitia, Montpellier,

France

[4] University of Stavanger, Faculty of Science and Technology, Department of Electrical

Engineering and Computer Science, Norway

[5] University of Stavanger, Faculty of Health Sciences, Department of Quality and Health

Technology, Norway

[*] Corresponding author: Valentin Geslin valentin.geslin@protonmail.com

1

Highlights

18   ●   New whole slide image analysis method applied to an oyster disease.

19   ●   This method is used to estimate bacteria spread into oyster's whole tissues.

20   ●   Bacteria quantification by this method is coherent with molecular results from

21   qPCR.

22   ●   The method brings new insights into *Vibrio aestuarianus* infection pattern.

Abstract

Growth of marine bivalve aquaculture is presented as a potential measure to effectively provide seafood for human consumption while preserving wild populations. It can be an economic driver in coastal areas while also providing important ecosystem services such as filtration of phytoplankton and carbonate buffering. However, as with any other farming practices, increased densities of individuals in a confined space often result in disease outbreaks. Pathogens developing in these conditions can easily spread among farmed stocks, affecting all the production lines and potentially causing adverse economic consequences, spreading over large areas and eventually affecting wild populations as well. Development and implementation of early detection methods for pathogen infection are imperative to maintain and expand aquaculture activities. In this context, a new method to quantify and characterize infection by *Vibrio aestuarianus* in the Pacific oyster, *Magallana gigas*, based on image analysis of histological slides stained by immunohistochemistry is presented. The method is used to automatically measure the proportion of tissue infected by IHC-stain bacteria from each image and to characterize bacteria spread in the tissue. The proportion of tissue infected by IHC-stained bacteria and spatial dispersion indexes, used to characterize 2D bacterial dispersion, were directly associated with the quantity of bacteria previously measured by qPCR. All of these results suggest a pattern of infection where *V. aestuarianus* tends to be more clustered and less randomly spread in the organism with increased infection. Advantages, limitations, and potential ways to improve the method are discussed.

Keywords

44

45 Digital histopathology; Immunohistochemistry; *Magallana gigas*; *Vibrio aestuarianus*; Whole

46 slide image

1. Introduction

Emerging pathogens represent one of the most significant threats to the growth and sustainability of aquaculture industries worldwide (Lupo et al., 2016) and the outbreak of aquatic animal diseases related to intensive production practices is of major concern for the industry, local population living from this activity and the ecosystem (Boyd and Clay, 1998; Griffiths et al., 2018; Landos et al., 2021). Past severe disease outbreaks have led to significant economic destruction and negative social consequences (Carnegie et al., 2016). Disease outbreaks often occur from a combination of different factors such as climate change (Barange, 2018; Garrabou et al., 2022; Li et al., 2023; Wright et al., 2023), environmental pollution (Kalkan and Altuğ, 2020; Kathijotes et al., 2015; Landos et al., 2021), habitat alteration (Barange, 2018), geographic expansion of disease (Barange, 2018; Carnegie et al., 2016), and invasive species (Green et al., 2016; Wright et al., 2023; Yang et al., 2021). Aquaculture practices, which confine animals at high density in specific areas, and often involve manipulation and transfer of farmed animals from one location to another, are another source of stress which can entail conditions conducive to the outbreak and propagation of infectious agents (Carnegie et al., 2016; Palacios et al., 2010). All these factors can directly impact the prevalence and severity of disease outbreaks in both farmed and wild aquatic populations (Landos et al., 2021). In a world where the human population continues to grow, bivalve mollusc farming is a privileged sector due to the importance of these protein-rich animals for human consumption. In this context, aquaculture can play a strategic role in terms of safe food production and sustainable economic and social development (Noger-Huet et al., 2022; Petrosillo et al., 2023). The development of new methods for disease detection in marine shellfish is

70   essential to detect diseases as early as possible and apply contingency measures to

71   contain their spread to other aquaculture facilities (Carnegie et al., 2016).

72   The Pacific oyster *Magallana gigas*, indigenous to Northeast Asia, is the most cultivated

73   species in the world (Chaney and Gracey, 2011), including France, where the yearly

74   production in 2022 was estimated at 85,000 tons (FAO, 2022). Since the early 1990s,

75   Pacific oysters have been hit by mass mortality in many areas of the world (Arzul et al.,

76   2017; Burge et al., 2018; Castinel et al., n.d.; EFSA Panel on Animal Health and Welfare

77   (AHAW), 2015; McCombie and Samain, 2007; OIE, 2019). These outbreaks, either due

78   to the presence of the virus OsHV-1 or the bacteria *Vibrio aestuarianus*, have had a major

79   impact on oyster production in France and, also on a wider scale, in Europe (EFSA Panel

80   on Animal Health and Welfare (AHAW), 2015). Alarmingly, the prevalence of these

81   pathogens in European oyster populations appears to be increasing in the last decades

82   (Carnegie, 2020). Consequences of infection by *V. aestuarianus* on *M. gigas* range from

83   non-lethal to lethal effects, leading to behavioral change (Elston, 1993), pathological

84   reaction (Garnier et al., 2007), and ultimately to death (Parizadeh et al., 2018b). Oysters

85   are frequently moved between spat collection sites or hatcheries and oyster farming

86   locations in France, as well as between France and various European countries (Arzul et

87   al., 2022). Therefore, the lack of efficient transport control and detection systems can

88   contribute to the widespread transmission of pathogenic agents and diseases (Carnegie

89   et al., 2016; Fuhrmann et al., 2019). In this context, the development of analysis

90   techniques allowing early detection and accurate diagnosis of invasive species is one of

91   the major issues in the aquaculture sector. The main detection methods currently used to

92   assess *V. aestuarianus* infection in *M. gigas* are histopathological diagnosis together with

93 strain identification by polymerase chain reaction (PCR) and quantitative polymerase

94 chain reaction (qPCR) assays to quantify infection intensity (Carnegie, 2020).

95 Nevertheless, due to the short incubation time of the pathogenic agents (bacterial or viral)

96 and its rapid increase in prevalence level, it remains difficult to detect infection in advance

97 of a large-scale episode of disease by conventional surveillance methods (Parizadeh et

98 al., 2018a; Paul-Pont et al., 2013; Whittington et al., 2019).

99 Image analysis is rapidly evolving and increasingly used in histopathology as it enables

100 high throughput analysis of a large number of samples, offering the potential for increased

101 diagnostic precision, improved reproducibility, and potentially reduced workload for

102 histopathologists (Zarella et al., 2018). Production of whole slide images (WSI) involves

103 the scanning of a microscope slide to create a single high-resolution digital file. WSI are

104 pyramidal images of histological slides containing complex data and have a higher

105 resolution compared to a raster graphic file which allows the detection of cellular or even

106 sub-cellular structure (Bolte and Cordelières, 2006; Pantanowitz et al., 2011). Whole slide

107 imaging represents a paradigm shift in histopathology with potential impacts on

108 workflows, reproducibility, dissemination of educational material, and intra and inter-

109 institutional collaboration (Bolte and Cordelières, 2006). Although the benefits of WSI

110 analysis are numerous, implementing such methods on routine procedures remains slow

111 because it would require some adaptation and its complexity is still an obstacle to its

112 widespread adoption (Aeffner et al., 2019).

113 In this article, a method to detect, quantify and characterize *V. aestuarianus* infection of

114 *M. gigas* from WSI stained by immunohistochemistry (IHC) is proposed. *M. gigas* were

115 experimentally infected with *V. aestuarianus* to control and create different degrees of

7

116   infection (Parizadeh et al., 2018b). The method is based on the computerized detection

117   of *V. aestuarianus* stained by IHC within the WSI. The proportion of tissue infected by

118   IHC-stained bacteria is measured and spatial spreading within the cross-section is

119   characterized. Bacterial quantities assessed with this method are consistent with results

120   obtained by qPCR and the method brings new details on bacterial spreading behavior.

121   2.   Material & Method

122   WSI and qPCR results originated from Parizadeh (2018). WSIs were produced to

123   assess histopathological damages in *M. gigas* infected under experimental conditions

124   by *V. aestuarianus* against the degree of bacterial infection assessed by quantitative

125   polymerase chain reaction (qPCR) and immunohistochemistry with the use of a

126   polyclonal antibody (Parizadeh et al., 2018b). To summarize the original experimental

127   set-up, specimens of *M. gigas* were immersed in a bacterial bath for different periods to

128   simulate different levels of bacterial infection and individuals were sampled at different

129   time points after infection (day 1 and day 4). Histopathological damages and localisation

130   of IHC-stained *V. aestuarianus* in different tissues were assessed by histology on

131   hematoxylin-eosin (H&E) stain slides and slides stained by IHC with a bacteria-specific

132   polyclonal antibody. The dataset consists of 41 images of histological cross-section of

133   *M. gigas* stained with H&E for histopathological assessment and 41 images of

134   histological cross-section of *M. gigas* stained with IHC for localisation of the bacteria

135   and 230 bacterial DNA quantification performed on different tissue (gills, digestive

136   gland, mantle, abductor muscle, labial palp) from 43 specimens. qPCR results were

137   treated individually by tissue and the overall mean was calculated for every specimen.

138   Logarithm-transformed values were used for qPCR values. Only specimens with both

139   image and qPCR data were integrated into the current analysis (n = 38). Samples were

140   classified into 3 infection groups according to the level of bacteria measured by qPCR,

141   with the "control group" encompassing every control specimen, samples with a level of

142   bacteria cells per animal ranging from 0 to 1.10^5 bacteria/25 ng of total DNA, falls into

143   "early infection group", and "advanced infection group" encompass samples presenting

144   a level of bacteria cells above 1.10^5 bacteria per 25 ng of total DNA. See Table 3 and

145   Figure A in 7.0 Supplementary Material.

146   Original WSI and qPCR data can be found here:

147   https://www.seanoe.org/data/00501/61299/

148   Software used for image analysis were QuPath (0.5.1), Python (3.11.5) and Fiji (2.15.0).

149   QuPath is an open-source bioimage analysis software for digital pathology and whole

150   slide image analysis (https://qupath.github.io/). Python is a general-purpose, object-

151   oriented programming language, it offers a comprehensive standard library to work on

152   different types of objects (https://www.python.org/). Fiji is an image processing package

153   distribution of ImageJ2 (https://imagej.net/software/fiji/).

154
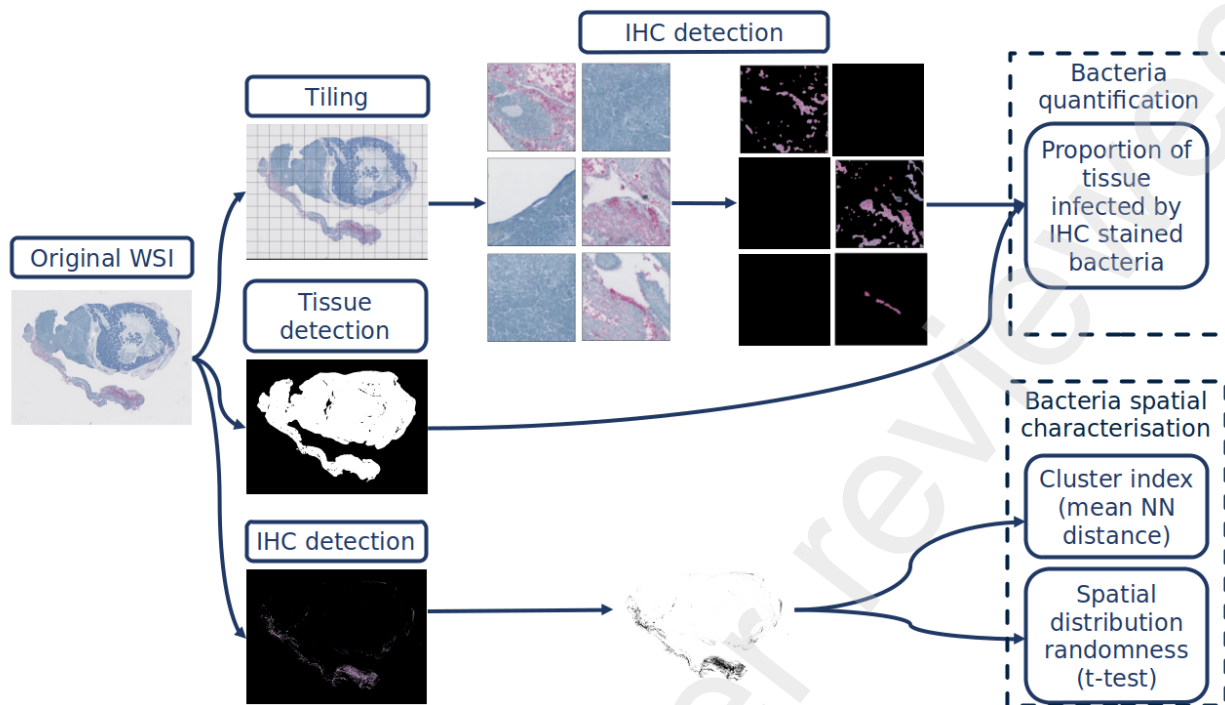
Figure 1: General workflow of the WSI analysis automated method. WSIs are fragmented into tiles for IHC detection

analysis. In parallel, tissue detection is performed to get the overall tissue area per image to compute the proportion

of tissue area infected by IHC-stained bacteria. IHC-stained bacteria particles are extracted from the WSI and used to

perform colocalization and spatial distribution analysis.

Tissue detection was performed using a thresholding method in QuPath (see Method

calibration for more details). Pixel dimensions were exported from QuPath for each

WSI's metadata. Tiles of a specific size (400 μm^2) with a downsampling factor of 1 were

generated within the area of tissue detected for each WSI and exported as raster

graphics files. Tiles were converted from RGB to HSV, a lower and upper color range

corresponding to IHC stained color were defined in Python. Color thresholding was

performed on each tile to obtain a binary mask that selects only pixels within the defined

range by lower and upper values. Black pixels are the pixels falling outside the defined

color range and therefore were assumed to represent tissue with no IHC-stained

bacteria present, while non-black pixels are the pixels falling within the IHC color

10

169   threshold range and were assumed to represent tissue infected by IHC-stained bacteria.

170   Some tiles from different tissues and their respective masks are presented in Table 1.

171   The number of non-black pixels was exported for every masked tile. The area of tissue

172   infected by IHC-stained bacteria was calculated by multiplying the number of non-black

173   pixels by the pixel dimensions for all tiles and summing them for each image. Values of

174   IHC-stained bacteria area were corrected by subtracting the highest area measured in

175   the "control" group from every sample. Specimens from "control" are assumed not to

176   have been infected by *V. aestuarianus* and therefore all IHC detected in these samples

177   are considered as artefacts.

178   WSIs were exported as raster images with HistoQC (Janowczyk et al., 2019). HistoQC

179   is an open-source tool written in Python used to identify artefact-free areas on digitized

180   slides. These images were used to characterize IHC-stained bacteria colocalization

181   and spatial dispersion within the whole cross-section. Particle distribution analysis

182   statistically determines if particles in each image are likely to be randomly distributed,

183   self-avoiding or clustered. The "2D Particle Distribution" function from the BioVoxxel

184   plugin was used to characterize IHC stained particle spatial dispersion within the

185   images (Brocher, 2023). It calculates the nearest neighbor distance (NND) for each

186   particle and computes the theoretical NND. The measured mean NND is used as a

187   cluster index, it was statistically compared using a t-test to the theoretical mean NND to

188   determine particle distribution (Lagache et al., 2015) (Figure 1).

189   Statistical analysis was performed using R (version 4.3.1). A 0.05 significance level was

190   used for all statistical tests. Wilcoxon test is a non-parametric test used to determine if

191   two independent groups present a significant difference in their median value. Wilcoxon

11

192   test was used to determine if the median of the distribution from the proportion of tissue

193   infected by IHC stained bacteria, mean quantity of bacteria cells, mean NND and spatial

194   dispersion indexes were significantly different from 0. Kruskal-Wallis test followed by

195   Dunn's test was used to compare the proportion of tissue infected by IHC-stained

196   bacteria, mean NND and spatial dispersion index, between infection groups. The

197   Kruskal-Wallis test is a non-parametric test used to reveal statistically significant

198   differences between the medians of several independent groups. Dunn's test performs

199   pairwise comparisons between each independent group and tells which groups are

200   statistically significantly different. Kendall correlation test was used to assess the linear

201   relationship between bacterial quantity and, the proportion of tissue infected by IHC-

202   stained bacteria in each image as well as the relationship between the proportion of

203   tissue infected by IHC-stained bacteria and with spatial dispersion index. Logarithmic

204   regressions were used to model the relationship between the mean quantity of bacteria

205   (log10) per sample, as a predictor variable, the proportion of tissue infected by IHC-

206   stained bacteria, as well as the relationship between the proportion of tissue infected by

207   IHC-stained bacteria and the dispersion index. The F-value tells whether the regression

208   model provides a better fit to the actual data than a model with no predictor variables.

209   All scripts used for image and data analysis are available on the following repository:

210   https://github.com/ValentinGeslin/OYSTER

211   ## 2.1.   Method calibration
212   ### 2.1.1.   Colocalization
213   Colocalization is the spatial correlation between objects, it reveals whether different

214   objects are localized within a certain area or not. It was used to assess if detected IHC-

215   stained bacteria were localized within the tissue or not. Characterisation of IHC-stained

216   bacteria colocalization within the whole tissue was performed on Fiji with the JaCoP

217   plugin using an object-based colocalization measurement (Bolte and Cordelières,

218   2006). Object-based colocalization measurements refer to a colocalization method

219   where objects of interest are first segmented from the image, then their spatial

220   relationships are measured. This type of colocalization method was used because it is

221   generally considered less sensitive to image noise and statistically more robust than

222   pixel-based methods (Lagache et al., 2015). Pearson's correlation coefficient was used

223   to express the correlation between colocalized objects, and the linear equation

224   describing the relationship between objects in IHC-detected images and mask tissue

225   images was calculated by a linear regression with the slope of the regression providing

226   the rate of association between the objects (Brocher, 2023). Pearson's coefficient

227   provides an estimate of the goodness of this approximation with its value ranging from 1

228   to -1, with 1 standing for complete positive correlation, 0 standing for no correlation, and

229   -1 for a negative correlation (Lagache et al., 2015). Pearson's correlation coefficient

230   represents the degree of colocalization. The colocalization coefficient ranges from -

231   0.006 to 0.356 with a median value of 0.007. Individual values can be found in Table 3

232   in 7.0 Supplementary Material. The median of Pearson's correlation coefficient exhibits

233   significant difference between the 3 groups (Kruskal-Wallis, p-value < 0.05). The

234   median colocalization index for the "control" and "early infection" group was not

235   significantly different from 0 (Wilcoxon test, p-value > 0.05) while "advanced infection"

236   has a median value of 0.20 (Figure 2).

13
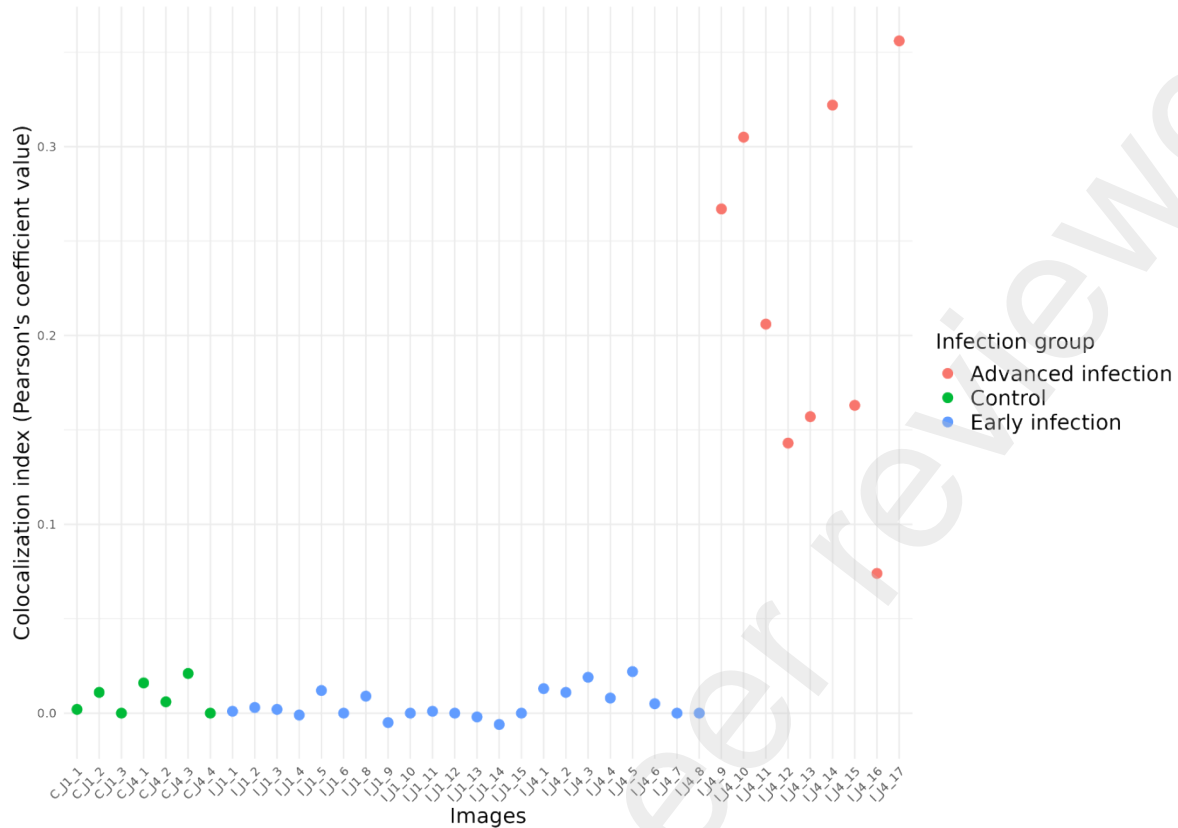
237
238 *Figure 2: Pearson's coefficient value per image and category. Pearson's coefficient value for the control and early*

239 *infection cohort ranges from -0.006 to 0.02, while for the advanced infection group Pearson's coefficient value ranges*

240 *from 0.07 to 0.35 with a median value of 0.20.*

241 ### 2.1.2. Tissue detection parameters

242 The influence of tissue detection parameters on the proportion of tissue positive to IHC-

243 stained bacteria was evaluated using 5 different sets of parameters which were judged

244 optimal by visual assessment. For all images, the detection of tissue infected by IHC-

245 stained bacteria was not significantly different for the 5 sets of parameters (Kruskal

246 Wallis test, p-value > 0.05).

247 ### 2.1.3. Tile size variability

248 Incidence of tile size variability on the proportion of tissue positive to IHC stained

249 bacteria was assessed for seven different tile sizes and no significant difference was

14

250 found (Kruskal Wallis test, p-value > 0.05), meaning that tile size does not significantly

251 influence detection and quantification of IHC stained *V. aestuarianus* in the images.

252 *Table 1: Some tiles from different tissues sorted by condition. On original tiles, different tissues (gills, digestive gland,*

253 *mantle, abductor muscle, labial palp) are visible with IHC-stained bacteria (pink color) when infected. Masked tiles*

254 *display only IHC-stained bacteria if present in the original tile.*

Infection status	Tile	Gills	Digestive gland	Mantle	Abductor muscle	Labial palp
Control	Original tile					
	Masked tile					
Early infection	Original tile					
	Masked tile					
Advanced infection	Original tile					
	Masked tile					

255

3. Results

3.1. Quantity of bacteria in whole organism

The quantity of bacteria in whole organisms was obtained by calculating the mean quantity of bacteria measured in different tissues (gills, digestive gland, mantle, muscle, and labial palp) for each specimen. The 3 conditions (control, early infection and advanced infection) reflect the quantity of bacteria distribution (Figure A - Supplementary Material) and they exhibit significant differences between them (Kruskal-Wallis test, p-value < 0.05) with the "control" group presenting a median quantity of bacteria cells per animals not significantly different from 0 (Wilcoxon test, p-value > 0.05) while the median quantity of bacteria cells per animals for "early infection" and "advanced infection" group were significantly higher than "control" group (Dunn's test, p-value < 0.05), with a median value of 0.46 for "early infection" group and 6.93 for "advanced infection" group (Figure 3).

3.2. Proportion of tissue infected by IHC-stained bacteria

The median value of the proportion of tissue infected by IHC-stained bacteria was significantly higher than 0 (Wilcoxon test, p-value < 0.05) for the 3 categories, with the "advanced infection" group being significantly higher than the two other groups (Dunn's test, p-value < 0.05). "Control" and "early infection" groups display the proportion of tissue infected by IHC-stained bacteria ranging from 0% to 0.09%, while the proportion of tissue infected by IHC-stained bacteria for the "advanced infection" group ranges from 1.47% to 26.53%, with a median value of 9.19% (Figure 3).

16
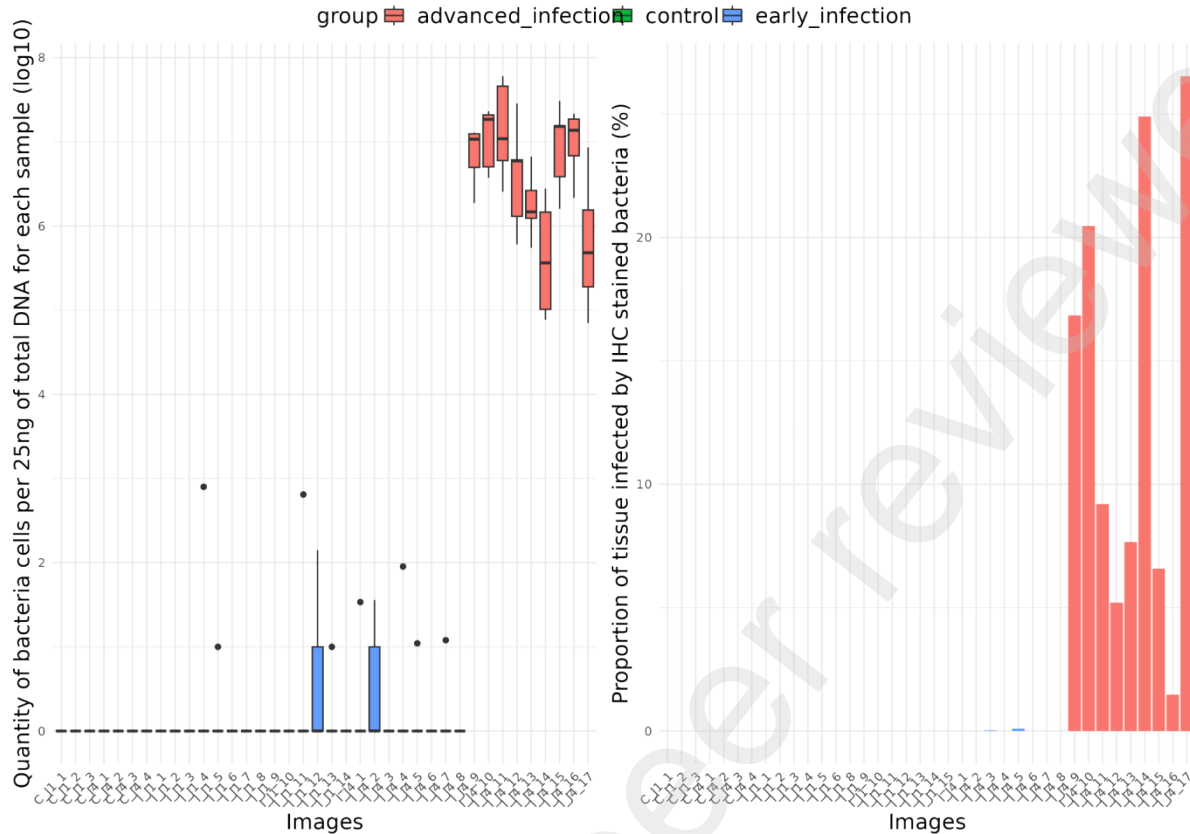
277
278 *Figure 3: Quantity of bacteria cells (log10) per 25ng of total DNA (left) and proportion of tissue area (%) infected by*

279 *IHC stained bacteria per images and for the different groups (right). The mean values of the quantity of bacteria cells*

280 *for the control, early infection and advanced infection groups were respectively 0, 0.46, and 6.82. With mean quantity*

281 *of bacteria cells from the control and early infection group being not significantly different from 0 (Wilcoxon test, p-*

282 *value < 0.05) and the advanced infection group being significantly higher than the 2 other groups (Dunn's test, p-*

283 *value > 0.05). The mean value of the proportion of tissue infected by IHC-stained bacteria for control, early infection*

284 *and advanced infection group are respectively 0%, 0.005% and 13.20%. The proportion of tissue area infected by*

285 *IHC-stained bacteria for the advanced infection group was significantly higher than the 2 other groups (Dunn's test, p-*

286 *value > 0.05). The advanced infection group significantly stands out from the 2 other groups for the quantity of*

287 *bacteria cells (log10) per sample and the proportion of tissue area (%) infected by IHC-stained bacteria per image.*

3.3. Relationship between quantity of bacteria and proportion of tissue infected by IHC stained bacteria per sample

A Spearman's rank correlation was used to test the strength and direction of the relationship between the proportion of tissue infected by IHC-stained bacteria and the mean quantity of bacteria measured by qPCR (Figure 4). A significant positive correlation was found between these two variables (tau = 0.59, p-value < 0.05). To better describe the monotonic relationship between the area of tissue infected by IHC-stained bacteria and the mean quantity of bacteria per sample the following logarithmic regression model was fitted to the data:

$$y = 3.42 + 0.59 * \ln(x)$$

The overall F-value of the model was 43.91 (p-value < 0.05) with an adjusted R squared of 0.53 (Figure 4).

18

301

302 *Figure 4: Relationship between proportion of tissue infected by IHC stained bacteria and mean quantity of bacteria*

303 *(log10) per image and category. Control and early infection samples display a relatively low proportion of tissue*

304 *infected by IHC-stained bacteria (min = 0%, max = 0.09%) and mean quantity of bacteria cells (min = 0, max = 2.20)*

305 *compared to the advanced infection group where values from the proportion of tissue infected by IHC stained*

306 *bacteria range from 1.47% to 26.53% and values from mean quantity of bacteria (log10) range from 6.01 to 7.39. The*

307 *overall F-value of the logarithmic regression model is 43.91 with a corresponding p-value lower than 0.05, which*

308 *indicates that the model fits the data.*

3.4. Spatial characterisation of IHC-stained bacterial infection

3.4.1. Spatial dispersion

312 The 3 conditions exhibit significant statistical differences between them for t-test value

313 (Kruskal-Wallis test, p-value < 0.05) representing whether or not spatial dispersion of

314 IHC stained bacteria follows a specific pattern or is random. "Control" and "early

315 infection" groups do not manifest significant differences between them (Dunn's test, p-

19

316 value > 0.05) while the "advanced infection" group presents a value significatively higher

317 than 0 (Wilcoxon test, p-value < 0.05). Values can be found in Table 3 in 7.0

318 Supplementary Material. A significant positive correlation was found between the

319 proportion of tissue infected by IHC-stained bacteria and t-test values (tau = 0.74, p-

320 value < 0.05).

321 ### 3.4.2. Cluster index

322 Another proxy used to assess and characterize bacterial dispersion is the cluster index,

323 it represents the average minimal distance between IHC-stained bacteria and therefore

324 if bacteria tend to form clusters or not. The standard deviation of the mean NND is

325 informative about spatial dispersion homogeneity, or if particles tend to be clustered

326 (lower standard deviation) or randomly dispersed (higher standard deviation). It ranges

327 from 82.49µm to 8862.10µm with a median value of 243.27µm, and from 89.01µm to

328 8342.25µm with a median value of 849.27µm respectively for the "control" and "early

329 infection" groups. Individuals from the "advanced infection" group present mean NDD

330 ranging from 46.81µm to 64.79µm with a median value of 54.40µm (Figure 5). Individual

331 values can be found in Table 3 in 7.0 Supplementary Material. A significant difference in

332 mean NDD value is observed between individuals from the advanced infection group

333 and the two other groups (Dunn test, p-value < 0.05) while the control and early

334 infection group do not present significant differences between them (Dunn test, p-value

335 > 0.05). The 3 infection groups exhibit a significant difference in their standard deviation

336 of mean NDD (Kruskal-Wallis test, p-value < 0.05). It indicates that bacteria in the

337 advanced infection stage tend to be more clustered than at an early infection stage

338 (Figure 5).

339
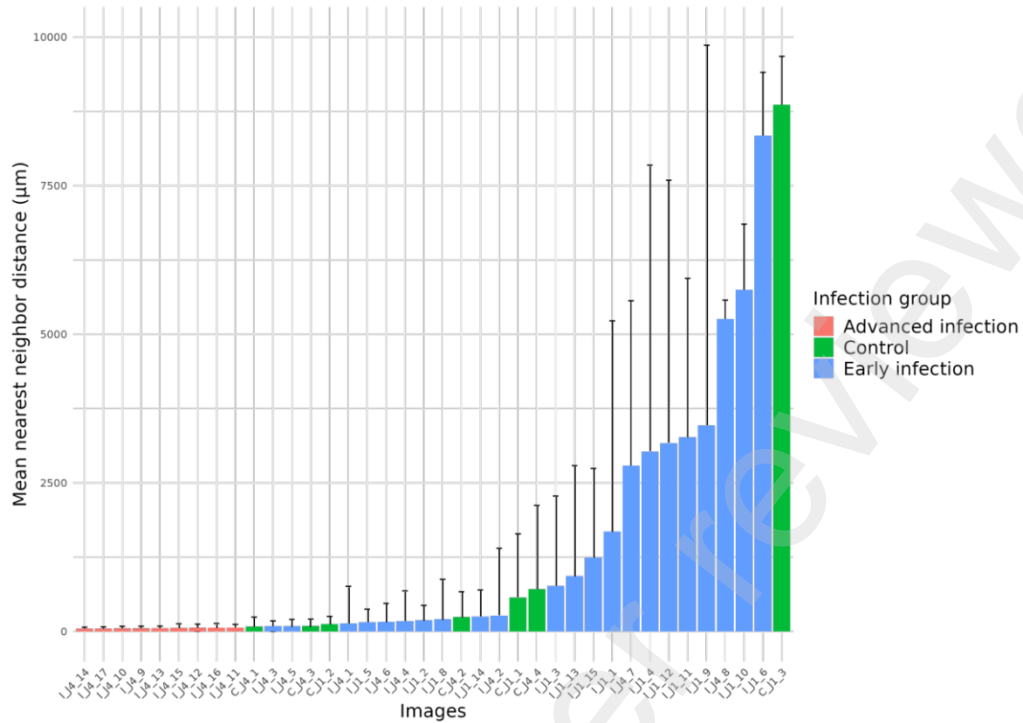
Figure 5: Distribution of mean nearest neighbor distance (NDD) between particles per sample infection status (left)

and mean NDD (with standard deviation) between particles per image and category (right). The mean NDD between

particles for the control and early infection cohort ranges from 82.49μm to 8862.10μm, while for the advanced

infection group values range from 46.81μm to 64.79μm with a median value of 54.40μm.

4. Discussion

In this article, an image analysis method to detect, quantify and characterize IHC-

stained *V. aestuarianus* infection from WSI of *M. gigas* was presented. The method is

based on the separation of IHC-stained bacteria from other features in the images and

its analysis. Different characteristics such as area, mean NDD and spatial dispersion of

IHC-stained bacteria are analyzed in each image and linked to the level of infection

measured by qPCR in the corresponding samples. Significant correlations were found,

and a logarithmic regression model fitting the data was computed. It supports the claim

that this image analysis method might be complementary to the qPCR method being

21

353 currently the gold standard to assess bacterial infection in *M. gigas*. Results from image

354 analysis methods generally conform to the results from the original research (Parizadeh

355 et al., 2018b). The spread and quantity of bacteria in tissue is positively associated with

356 the degree of bacterial infection (Parizadeh et al., 2018b). However, the image analysis

357 method allows a more detailed quantification and characterisation of this relationship.

358 The level of bacteria measured by qPCR is weakly related to the exposure duration.

359 Therefore, grouping the samples according to the level of bacterial infection rather than

360 their exposure duration seems to be more biologically relevant as *V. aestuarianus* is

361 suspected to have an asynchronous infection behavior, with an initial infection by a few

362 bacteria cells in the hemolymph where the bacteria will multiply until it reaches a critical

363 number of pathogenic cells who will then quickly colonize other tissue (Parizadeh et al.,

364 2018a). Results from the image analysis method are conformed to qPCR results; the

365 proportion of tissue infected by IHC-stained bacteria is positively related to the mean

366 quantity of bacteria. However, the quantities respectively quantified by the two methods

367 are not completely aligned. Despite that *V. aestuarianus* was not detected by qPCR in

368 individuals from the control group, the proportion of tissue infected by IHC-stained

369 bacteria was not equal to 0. On the contrary, significant bacterial level was detected in

370 some specimens from the "early infection" group, these same individuals do not exhibit

371 corresponding value of tissue area infected by IHC-stained bacteria. For some

372 specimens from "control" and "early infection" categories, small areas positive to IHC

373 stained bacteria were measured and bacteria-like cells were identified by visual

374 assessment; however these minute signs of bacterial presence within the tissues were

375 not always picked up by qPCR (Table 2). The opposite was also observed, in samples

22

376   where *V. aestuarianus* was detected by qPCR but not showing any signs of it on the

377   image (Table 1). On the other hand, the quantity of bacteria measured by qPCR in the

378   "advanced infection" cohort is significantly higher than in the two other groups and

379   similarly for the proportion of tissue infected by IHC-stained bacteria. The discrepancy

380   between qPCR results and the results obtained by image analysis could arise from

381   multiple factors. First, the quantity of bacteria considered in the analysis was obtained

382   by aggregating measurements performed in different tissues (gills, digestive gland,

383   mantle, muscle, labial palp) but as it was mentioned previously, *V. aestuarianus* is

384   suspected to have an asynchronous infection pattern, so its spread might not be similar

385   in the different tissue of *M. gigas* and as cross-section does not always contain the

386   same proportion of the different tissue, some organs might be under or over-

387   represented in the images (Zarella et al., 2018). Another factor to consider is that some

388   bacteria might be washed away during histological preparation, particularly because of

389   the poor conservation of circulatory fluids – haemolymph-, therefore bacterial infection

390   from the image analysis method might be underestimated. Finally, qPCR methods can

391   detect as few as 10^3 bacteria from small pieces of tissues (mg) (Saulnier et al., 2009).

392   But in the first infection steps, this analytical threshold can limit bacterial detection.

393   Despite these potential limitations, this finding supports that the image analysis method

394   could be complementary to qPCR as it has a good sensitivity to minute infection signs.

395   Mean NND and dispersion index were used to characterize bacterial spread in the

396   tissue. These two indicators were positively correlated to the proportion of tissue

397   infected by IHC-stained bacteria as well as the quantity of bacteria measured by qPCR.

398   It comforts the actual pathogenesis model for *V. aestuarianus* associated disease, *V.*

23

399 *aestuarianus* tends to develop in clusters with increased bacterial infection (Parizadeh

400 et al., 2018a). With this quantitative approach, we are now able to propose a spatial

401 representation of disease progression characterizing the spatial dynamics of infection of

402 *M. gigas* by *V. aestuarianus* on a fine scale. Based on this approach, pathogenesis

403 induced by *V. aestuarianus* in *M. gigas* can be summarized in several successive

404 stages: (1) initial penetration and colonization (2) bacterial multiplication at entry sites

405 (3) dispersion and invasion of connective tissues. Finally, the progression of the disease

406 was associated with an increase in bacterial clusters in all the animal tissues, confirming

407 the septicemic characteristics of *V. aestuarianus* infection (Figure 6).

408

	First contact 1	Early stage of infection 2		Advanced stage of infection 3	
Biological pathway of infection	First contact host-pathogen	Penetration & early colonization	Incubation & multiplication	Multiplication & invasion	Lethal septicemia
qPCR Mean bacterial concentration (Quantity of bacteria cells (log10) per 25ng of total DNA)		0-10	10-10^4		>10^7
WSI Proportion of infected tissues (%)		0	0-0.1		1-30
WSI Spatial distribution Cluster index Randomness		Not clustered Random	Not clustered Random		Clustered Non Random

409 *Figure 6: Schematic representation of the different stages of pathogenesis and biological pathway of infection*

410 *induced by V. aestuarianus in M. gigas based on the WSI method combined with qPCR.*

4.1.   Limitations and potential ways for improvement

412 Digital pathology offers several potential benefits over traditional histopathological

413 methods and provides solutions to some of the key issues associated with the manual

24

414   assessment of tissue samples (Madabhushi and Lee, 2016). However, limitations

415   inherent to digital slide image analysis need to be addressed before further spreading of

416   the method and adoption into routine procedures. Pre-analytical steps are prone to

417   artifact generation including improper tissue placement (folding, tearing, air bubbles),

418   improper reagents (over or under-staining, stain batch variation), and poor microtomy

419   (thickness variances, knife chatter) (Aeffner et al., 2017). Slides digitization also

420   represents another potential source of artifacts generation, such as blurriness, lighting,

421   and contrast issues (Mulrane et al., 2008). Most of these pre-analytical steps can be

422   automatized and standardized to decrease the degree of variability and the odds of

423   artifact generation (Webster and Dunstan, 2014). Therefore, process automatization

424   and standardization should be encouraged in routine analysis, along with appropriate

425   quality control procedures to assess potential bias throughout the workflow (Aeffner et

426   al., 2019). Ideally, an experienced pathologist should stay involved in the whole analysis

427   and perform different quality control procedures along the workflow to assess the

428   influence of the different factors potentially interfering with the analysis (Carnegie et al.,

429   2016). A potential way to improve the method would be to analyze the different tissues

430   present in the WSI separately using a tissue detection method before the analysis

431   (Bándi et al., 2017). It could potentially help to improve the method by refining bacterial

432   infection at the tissue level instead of cross-section as it is now, and it could bring more

433   insight into pathogenesis and intra-inter organ infection patterns.

434   Another limitation comes from the problem of estimating the abundance of IHC stains in

435   histological tissue. As previously mentioned, the color range defined by upper and lower

436   HSV values to detect IHC-stained bacteria is arbitrary and relies only on expert

25
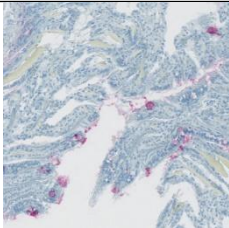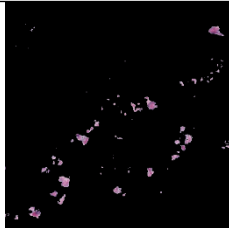
437 assessment. Extending or on the contrary reducing the threshold color range will affect

438 the number of pixels detected and ultimately the area covered by IHC-stained bacteria

439 detected in the images. Threshold values used for tissue detection and IHC detection

440 are subjective as it was determined by trial-and-error, and chosen parameters were the

441 ones giving the most satisfactory results in terms of tissue detected, artifacts removal

442 and IHC detection according to the operator. As it has been extensively documented,

443 visual assessment by pathologists can be influenced by inherent cognitive and visual

444 biases (Wolf et al., 2015). Therefore, running a sensitivity test on each of these

445 parameters before the analysis could help to build more objective tools to set these

446 parameters.
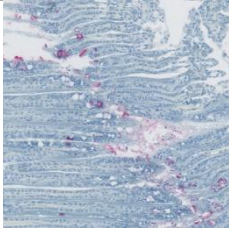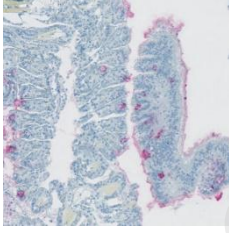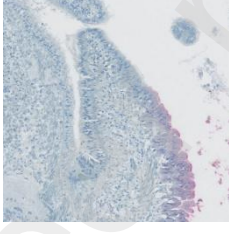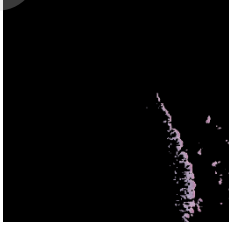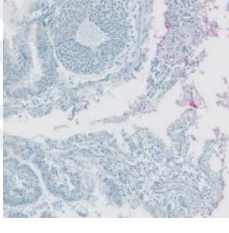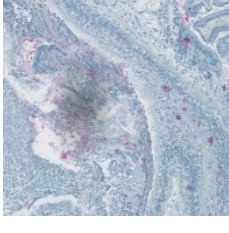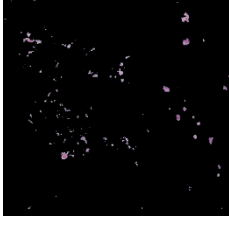
447 Further research should be carried out to validate the assumption that IHC-stained

448 bacteria detected on the slide are representative and, in some way, quantitatively

449 related to the abundance of the antigen present in the tissue section, which in turn is

450 related to the absolute number of bacteria in the original tissue (Taylor and Levenson,

451 2006). Moreover, this method quantifies bacterial spread only on a small portion of the

452 organ as a 2D slide is not representative of the complexity of an entire organ. Bacterial

453 infection dynamics in an organ and a whole organism might be more complex than what

454 the method can reveal from a single cross-section. Although the existence of an

455 inherent bias, if acknowledged and taken into consideration, might not limit the use of

456 the method as the results can be considered relative and not absolute, it would already

457 constitute a significant improvement compared to the qualitative assessment given by

458 traditional methods. Implementation of WSI is a multifaceted and inherently

459 multidisciplinary endeavor requiring contributions from different fields. Improved

26

460   understanding of current challenges to implementation, as well as the benefits of this

461   kind of method, can help prospective users identify the best means to achieve their

462   goals.

463   Another important aspect of the methodology presented here is that it relies solely on

464   open-source software, and the code was made publicly available through an online

465   repository. Privileging open-source and open-access material was done to promote the

466   development and use of such image analysis methods in the field of environmental

467   histopathology. Moreover, it could facilitate method improvement and implementation in

468   routine analysis. This image analysis method seems at least as efficient as the qPCR

469   method to detect and quantify bacterial infection in *M. gigas*, and its usage could

470   potentially be adopted in routine tests to improve early detection of *V. aestuarianus*

471   outbreak in aquaculture facilities. However, pre-analytical steps in WSI preparation

472   need to be standardized as these steps are prone to artifact generation and may

473   generate variability in the outcome and further research should be carried out on the

474   early infection phase to elucidate the dissimilarity between bacterial quantity measured

475   by qPCR and the proportion of tissue infected by IHC stained.

476   *Table 2: Examples of tiles from early infection groups showing evidence of bacterial infection and their respective*

477   *mask.*

Image	Infection status	Original tile	Masked tile
16049-8-3401002	Control		

16049-8-3401002	Control		
16049-8-3401002	Control		
16049-6-3301002	Control		
16049-6-3301002	Control		
16049-6-3301002	Control		

5. Acknowledgement

28

6. References

Aeffner, F., Wilson, K., Martin, N.T., Black, J.C., Hendriks, C.L.L., Bolon, B., Rudmann, D.G., Gianani, R., Koegler, S.R., Krueger, J., Young, G.D., 2017. The Gold Standard Paradox in Digital Image Analysis: Manual Versus Automated Scoring as Ground Truth. Archives of Pathology & Laboratory Medicine 141, 1267–1275. https://doi.org/10.5858/arpa.2016-0386-RA

Aeffner, F., Zarella, M.D., Buchbinder, N., Bui, M.M., Goodman, M.R., Hartman, D.J., Lujan, G.M., Molani, M.A., Parwani, A.V., Lillard, K., Turner, O.C., Vemuri, V.N.P., Yuil-Valdes, A.G., Bowman, D., 2019. Introduction to Digital Image Analysis in Whole-slide Imaging: A White Paper from the Digital Pathology Association. Journal of Pathology Informatics 10, 9. https://doi.org/10.4103/jpi.jpi_82_18

Arzul, I., Corbeil, S., Morga, B., Renault, T., 2017. Viruses infecting marine molluscs. Journal of Invertebrate Pathology, Invertebrate Viruses and the Food Chain 147, 118–135. https://doi.org/10.1016/j.jip.2017.01.009

Arzul, I., Garcia, C., Chollet, B., Serpin, D., Lupo, C., Noyer, M., Tourbiez, D., Berland, C., Dégremont, L., Travers, M.-A., 2022. First characterization of the parasite Haplosporidium costale in France and development of a real-time PCR assay for its rapid detection in the Pacific oyster, Crassostrea gigas. Transboundary and Emerging Diseases 69, e2041–e2058. https://doi.org/10.1111/tbed.14541

Bándi, P., van de Loo, R., Intezar, M., Geijs, D., Ciompi, F., van Ginneken, B., van der Laak, J., Litjens, G., 2017. Comparison of different methods for tissue segmentation in histopathological whole-slide images, in: 2017 IEEE 14th International Symposium on Biomedical Imaging (ISBI 2017). Presented at the 2017 IEEE 14th International Symposium on Biomedical Imaging (ISBI 2017), pp. 591–595. https://doi.org/10.1109/ISBI.2017.7950590

Barange, M., 2018. Impacts of climate change on fisheries and aquaculture. FAO ;

Bolte, S., Cordelières, F.P., 2006. A guided tour into subcellular colocalization analysis in light microscopy. Journal of Microscopy 224, 213–232. https://doi.org/10.1111/j.1365-2818.2006.01706.x

Boyd, C.E., Clay, J.W., 1998. Shrimp Aquaculture and the Environment. Scientific American 278, 58–65.

Brocher, J., 2023. biovoxxel/BioVoxxel-Toolbox: BioVoxxel Toolbox v2.6.0. https://doi.org/10.5281/zenodo.10050002

Burge, C.A., Ben-Horin, T., Bushek, D., Groner, M.L., Proestou, D.A., Huey, L.I., Bidegain, G., Carnegie, R.B., 2018. Intensive oyster aquaculture can reduce disease impacts on sympatric wild oysters. Aquaculture Environment Interactions 10, 557–567. https://doi.org/10.3354/aei00290

Carnegie, R., 2020. Working Group on Pathology and Diseases of Marine Organisms (WGPDMO). https://doi.org/10.17895/ICES.PUB.6086

Carnegie, R.B., Arzul, I., Bushek, D., 2016. Managing marine mollusc diseases in the context of regional and international commerce: policy issues and emerging concerns. Philosophical Transactions of the Royal Society B: Biological Sciences 371, 20150215. https://doi.org/10.1098/rstb.2015.0215

Castinel, A., Fletcher, Dhand, N., Rubio, A., Whittington, R.J., n.d. OsHV-1 mortalities in

527   Pacific oysters in Australia and New Zealand: the farmer's story. (No. 2567).

528 Chaney, M.L., Gracey, A.Y., 2011. Mass mortality in Pacific oysters is associated with a
529   specific gene expression signature. Molecular Ecology 20, 2942–2954.
530   https://doi.org/10.1111/j.1365-294X.2011.05152.x

531 EFSA Panel on Animal Health and Welfare (AHAW), 2015. Oyster mortality. EFSA
532   Journal 13, 4122. https://doi.org/10.2903/j.efsa.2015.4122

533 Elston, R.A., 1993. Infectious diseases of the Pacific oyster, Crassostrea gigas. Annual
534   Review of Fish Diseases 3, 259–276. https://doi.org/10.1016/0959-
535   8030(93)90038-D

536 FAO, 2022. The State of World Fisheries 2022 | FAO | Food and Agriculture
537   Organization of the United Nations [WWW Document].
538   https://doi.org/10.4060/cc0461en

539 Fuhrmann, M., Castinel, A., Cheslett, D., Furones Nozal, D., Whittington, R.J., 2019.
540   The impacts of ostreid herpesvirus 1 microvariants on Pacific oyster aquaculture
541   in the Northern and Southern Hemispheres since 2008. Impacto de
542   microvariantes del herpesvirus de los ostreidos 1 en el cultivo de ostra japonesa
543   en los hemisferios Norte y Sur desde 2008.
544   https://doi.org/10.20506/rst.38.2.3000

545 Garnier, M., Labreuche, Y., Garcia, C., Robert, M., Nicolas, J.-L., 2007. Evidence for the
546   Involvement of Pathogenic Bacteria in Summer Mortalities of the Pacific Oyster
547   Crassostrea gigas. Microb Ecol 53, 187–196. https://doi.org/10.1007/s00248-
548   006-9061-9

549 Garrabou, J., Gómez-Gras, D., Medrano, A., Cerrano, C., Ponti, M., Schlegel, R.,
550   Bensoussan, N., Turicchia, E., Sini, M., Gerovasileiou, V., Teixido, N., Mirasole,
551   A., Tamburello, L., Cebrian, E., Rilov, G., Ledoux, J.-B., Souissi, J.B., Khamassi,
552   F., Ghanem, R., Benabdi, M., Grimes, S., Ocaña, O., Bazairi, H., Hereu, B.,
553   Linares, C., Kersting, D.K., la Rovira, G., Ortega, J., Casals, D., Pagès-Escolà,
554   M., Margarit, N., Capdevila, P., Verdura, J., Ramos, A., Izquierdo, A., Barbera,
555   C., Rubio-Portillo, E., Anton, I., López-Sendino, P., Díaz, D., Vázquez-Luis, M.,
556   Duarte, C., Marbà, N., Aspillaga, E., Espinosa, F., Grech, D., Guala, I., Azzurro,
557   E., Farina, S., Cristina Gambi, M., Chimienti, G., Montefalcone, M., Azzola, A.,
558   Mantas, T.P., Fraschetti, S., Ceccherelli, G., Kipson, S., Bakran-Petricioli, T.,
559   Petricioli, D., Jimenez, C., Katsanevakis, S., Kizilkaya, I.T., Kizilkaya, Z.,
560   Sartoretto, S., Elodie, R., Ruitton, S., Comeau, S., Gattuso, J.-P., Harmelin, J.-
561   G., 2022. Marine heatwaves drive recurrent mass mortalities in the
562   Mediterranean Sea. Global Change Biology 28, 5708–5725.
563   https://doi.org/10.1111/gcb.16301

564 Green, T.J., Vergnes, A., Montagnani, C., de Lorgeril, J., 2016. Distinct immune
565   responses of juvenile and adult oysters (Crassostrea gigas) to viral and bacterial
566   infections. Vet Res 47, 72. https://doi.org/10.1186/s13567-016-0356-7

567 Griffiths, D., Pratoomyot, J., Vu, N.T., Jiravanichpaisal, P., Shinn, A.P., Briggs, M.,
568   Trong, T.Q., 2018. Asian shrimp production and the economic costs of disease.
569   Asian Fisheries Science Journal.

570 Janowczyk, A., Zuo, R., Gilmore, H., Feldman, M., Madabhushi, A., 2019. HistoQC: An
571   Open-Source Quality Control Tool for Digital Pathology Slides. JCO Clin Cancer
572   Inform 3, CCI.18.00157. https://doi.org/10.1200/CCI.18.00157

573 Kalkan, S., Altuğ, G., 2020. The composition of cultivable bacteria, bacterial pollution,
574   and environmental variables of the coastal areas: an example from the
575   Southeastern Black Sea, Turkey. Environ Monit Assess 192, 356.
576   https://doi.org/10.1007/s10661-020-08310-5
577 Kathijotes, N., Alam, L., Kontou, A., 2015. Aquaculture, coastal pollution and the
578   environment, in: Aquaculture Ecosystems. John Wiley & Sons, Ltd, pp. 139–163.
579   https://doi.org/10.1002/9781118778531.ch5
580 Lagache, T., Sauvonnet, N., Danglot, L., Olivo-Marin, J.-C., 2015. Statistical analysis of
581   molecule colocalization in bioimaging. Cytometry Part A 87, 568–579.
582   https://doi.org/10.1002/cyto.a.22629
583 Landos, M., Smith, M.L., Immig, J., 2021. Aquatic Pollutants in Oceans and Fisheries |
584   IPEN.
585 Li, X., Shi, C., Yang, B., Li, Q., Liu, S., 2023. High temperature aggravates mortalities of
586   the Pacific oyster (*Crassostrea gigas*) infected with *Vibrio*: A perspective from
587   homeostasis of digestive microbiota and immune response. Aquaculture 568,
588   739309. https://doi.org/10.1016/j.aquaculture.2023.739309
589 Lupo, C., Osta Amigo, A., Fleury, E., Robert, S., Garcia, C., Arzul, I., Baillon, L.,
590   Bechemin, C., Canier, L., Chollet, B., Dechamps, L., Dubreuil, C., Faury, N.,
591   Francois, C., Godfrin, Y., Lapegue, S., Morga, B., Travers, M.-A., Tourbiez, D.,
592   Masson, J.-C., Verin, F., Cordier, R., Gangnery, A., Louis, W., Mary, C.,
593   Normand, J., Penot, J., Cheve, J., Dagault, F., Le Jolivet, A., Le Gal, D., Lebrun,
594   L., Bellec, G., Bouget, J.-F., Cochennec-Laureau, N., Palvadeau, H., Grizon, J.,
595   Chabirand, J.-M., Pepin, J.-F., Seugnet, J.-L., D'Amico, F., Maurer, D., Le Gall,
596   P., Mortreux, S., Baldi, Y., Orsoni, V., Bouchoucha, M., Le Roy, V., Pouvreau, S.,
597   Queau, I., Lamoureux, A., 2016. Bilan 2015 du dispositif national de surveillance
598   de la santé des mollusques marins.
599 Madabhushi, A., Lee, G., 2016. Image analysis and machine learning in digital
600   pathology: Challenges and opportunities. Medical Image Analysis, 20th
601   anniversary of the Medical Image Analysis journal (MedIA) 33, 170–175.
602   https://doi.org/10.1016/j.media.2016.06.037
603 McCombie, H., Samain, J.-F., 2007. Summer mortality of Pacific oyster Crassostrea
604   gigas : The Morest Project 1–400.
605 Mulrane, L., Rexhepaj, E., Penney, S., Callanan, J.J., Gallagher, W.M., 2008.
606   Automated image analysis in histopathology: a valuable tool in medical
607   diagnostics. Expert Review of Molecular Diagnostics 8, 707–725.
608   https://doi.org/10.1586/14737159.8.6.707
609 Noger-Huet, É., Vagner, M., Le Grand, F., Graziano, N., Bideau, A., Brault-Favrou, M.,
610   Churlaud, C., Bustamante, P., Lacoue-Labarthe, T., 2022. Risk and benefit
611   assessment of seafood consumption harvested from the Pertuis Charentais
612   region of France. Environmental Pollution 292, 118388.
613   https://doi.org/10.1016/j.envpol.2021.118388
614 OIE, 2019. OIE - Annual report 2019 | Organisation mondiale de la santé animale. URL
615   https://report.oie.int/2019/en/ (accessed 5.9.24).
616 Palacios, G., Lovoll, M., Tengs, T., Hornig, M., Hutchison, S., Hui, J., Kongtorp, R.-T.,
617   Savji, N., Bussetti, A.V., Solovyov, A., Kristoffersen, A.B., Celone, C., Street, C.,
618   Trifonov, V., Hirschberg, D.L., Rabadan, R., Egholm, M., Rimstad, E., Lipkin,

619   W.I., 2010. Heart and Skeletal Muscle Inflammation of Farmed Salmon Is
620   Associated with Infection with a Novel Reovirus. PLOS ONE 5, e11487.
621   https://doi.org/10.1371/journal.pone.0011487

622 Pantanowitz, L., Valenstein, P.N., Evans, A.J., Kaplan, K.J., Pfeifer, J.D., Wilbur, D.C.,
623   Collins, L.C., Colgan, T.J., 2011. Review of the current state of whole slide
624   imaging in pathology. J Pathol Inform 2, 36. https://doi.org/10.4103/2153-
625   3539.83746

626 Parizadeh, L., Tourbiez, D., Garcia, C., Haffner, P., Dégremont, L., Le Roux, F.,
627   Travers, M.-A., 2018a. Ecologically realistic model of infection for exploring the
628   host damage caused by Vibrio aestuarianus. Environmental Microbiology 20,
629   4343–4355. https://doi.org/10.1111/1462-2920.14350

630 Parizadeh, L., Travers, M.-A., Garcia, C., Chollet, B., 2018b. Tissue damage and tissue
631   localisation of the bacteria Vibrio aestuarianus during an experimental infection
632   (oyster Crassostrea gigas). https://doi.org/10.17882/61299

633 Paul-Pont, I., Dhand, N.K., Whittington, R.J., 2013. Spatial distribution of mortality in
634   Pacific oysters Crassostrea gigas: reflection on mechanisms of OsHV-1
635   transmission. Diseases of Aquatic Organisms 105, 127–138.
636   https://doi.org/10.3354/dao02615

637 Petrosillo, I., Scardia Scardia, A.M., Ungaro, N., Specchiulli, A., Fanelli, G., Centoducati,
638   G., De Serio, F., Carlucci, R., Valente, D., Barbone, E., Pini, A., Giannuzzi, C.G.,
639   Scirocco, T., Lovello, E.M., Deflorio, M., Lillo, A.O., De Padova, D., Papa, L.,
640   Goffredo, E., Mancini, M.E., Mossa, M., 2023. Towards sustainable marine
641   spatial planning of aquaculture. Ecological Indicators 154, 110542.
642   https://doi.org/10.1016/j.ecolind.2023.110542

643 Saulnier, D., De Decker, S., Haffner, P., 2009. Real-time PCR assay for rapid detection
644   and quantification of Vibrio aestuarianus in oyster and seawater: A useful tool for
645   epidemiologic studies. Journal of Microbiological Methods 77, 191–197.
646   https://doi.org/10.1016/j.mimet.2009.01.021

647 Taylor, C.R., Levenson, R.M., 2006. Quantification of immunohistochemistry—issues
648   concerning methods, utility and semiquantitative assessment II. Histopathology
649   49, 411–424. https://doi.org/10.1111/j.1365-2559.2006.02513.x

650 Webster, J.D., Dunstan, R.W., 2014. Whole-Slide Imaging and Automated Image
651   Analysis: Considerations and Opportunities in the Practice of Pathology. Vet
652   Pathol 51, 211–223. https://doi.org/10.1177/0300985813503570

653 Whittington, R.J., Liu, O., Hick, P.M., Dhand, N., Rubio, A., 2019. Long-term temporal
654   and spatial patterns of *Ostreid herpesvirus 1* (OsHV-1) infection and mortality in
655   sentinel Pacific oyster spat (*Crassostrea gigas)* inform farm management.
656   Aquaculture 513, 734395. https://doi.org/10.1016/j.aquaculture.2019.734395

657 Wolf, J.C., Baumgartner, W.A., Blazer, V.S., Camus, A.C., Engelhardt, J.A., Fournie,
658   J.W., Frasca, S., Groman, D.B., Kent, M.L., Khoo, L.H., Law, J.M., Lombardini,
659   E.D., Ruehl-Fehlert, C., Segner, H.E., Smith, S.A., Spitsbergen, J.M., Weber, K.,
660   Wolfe, M.J., 2015. Nonlesions, Misdiagnoses, Missed Diagnoses, and Other
661   Interpretive Challenges in Fish Histopathology Studies: A Guide for Investigators,
662   Authors, Reviewers, and Readers. Toxicol Pathol 43, 297–325.
663   https://doi.org/10.1177/0192623314540229

664 Wright, A., Li, X., Yang, X., Soto, E., Gross, J., 2023. Disease prevention and mitigation

32

665 in US finfish aquaculture: A review of current approaches and new strategies.
666 Reviews in Aquaculture 15, 1638–1653. https://doi.org/10.1111/raq.12807
667 Yang, B., Zhai, S., Li, X., Tian, J., Li, Q., Shan, H., Liu, S., 2021. Identification of *Vibrio*
668 *alginolyticus* as a causative pathogen associated with mass summer mortality of
669 the Pacific Oyster (*Crassostrea gigas*) in China. Aquaculture 535, 736363.
670 https://doi.org/10.1016/j.aquaculture.2021.736363
671 Zarella, M.D., Bowman;, D., Aeffner, F., Farahani, N., Xthona;, A., Absar, S.F., Parwani,
672 A., Bui, M., Hartman, D.J., 2018. A Practical Guide to Whole Slide Imaging: A
673 White Paper From the Digital Pathology Association. Archives of Pathology &
674 Laboratory Medicine 143, 222–234. https://doi.org/10.5858/arpa.2018-0343-RA

7. Supplementary material

676
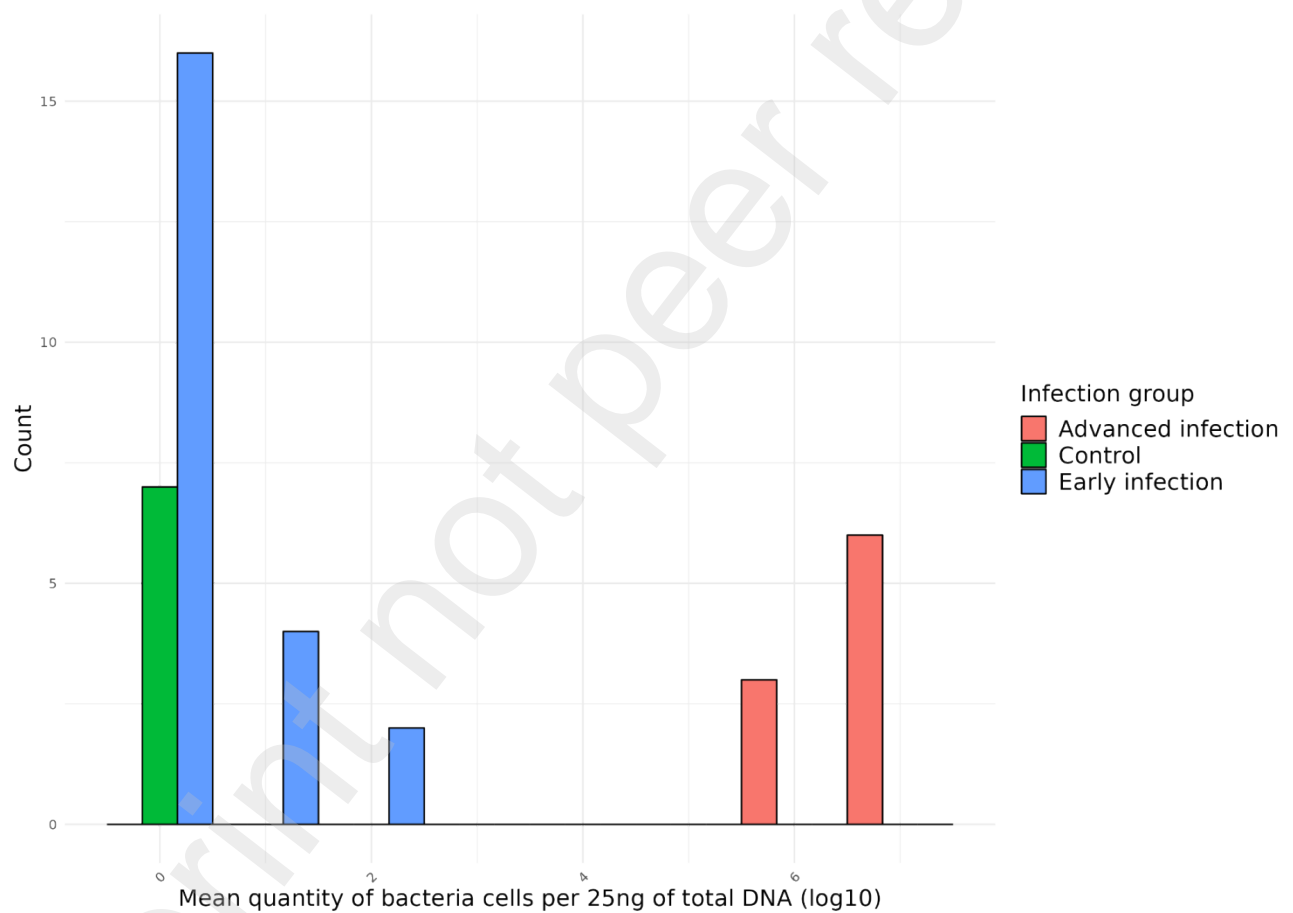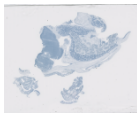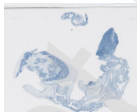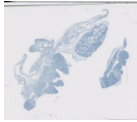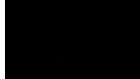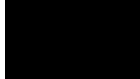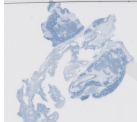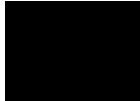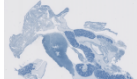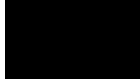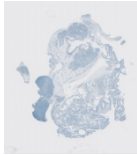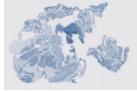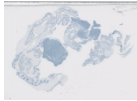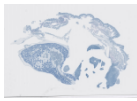
Figure A: Histogram of the quantity of bacteria (log10) measured by qPCR by group. All individuals from the control

group have a null level of bacteria cells. Individuals from the early infection group range from 0 to 2.9 with most of the

samples expressing a level of bacterial infection equal to 0. The level of bacterial infection in the advanced infection

group ranges from 1.19 to 17.81. The mean from the control and early infection groups are not significantly different
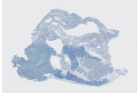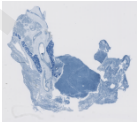
681   *while the mean of the advanced infection group was significantly different from the two other groups (Dunn's test - p-*

682   *value < 0.05).*

Table 3: Samples information
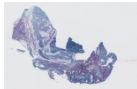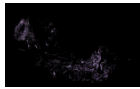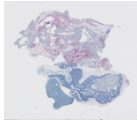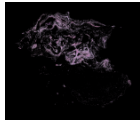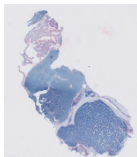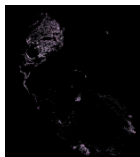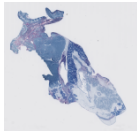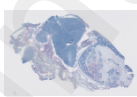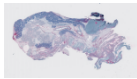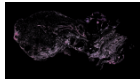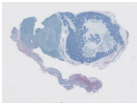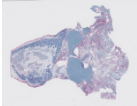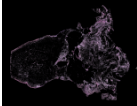
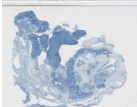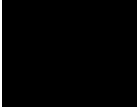| Sample name	Code image	Original image	Image of IHC stain bacteria detected	Treatment	Infection status	Mean bacterial quantity (log10) / (sd)	Proportion of tissue infected by IHC stained bacteria (%)	Colocalization coefficient (Pearson's correlation value)	Dispersion coefficient (t-test value)	Mean nearest neighbor distance value (µm)
16045-1-101002	I_J1_1			Infected J1	Early infection	0 (0)	2.86e-03	0.001	79.60	1681.38
16045-2-16110141B00901002	I_J1_2			Infected J1	Early infection	0 (0)	2.53e-02	0.003	128.67	189.19
16045-3-16110141B01001002	I_J1_3			Infected J1	Early infection	0 (0)	1.48e-02	0.002	86.016	766.06

16045-4-201002	I_J1_4			Infected J1	Early infection	2.20 (3.559820e+02)	1.51e-04	-0.001	77.087	3026.11
16045-5-16110141B01101002	I_J1_5			Infected J1	Early infection	0.30 (4.472136e+00)	4.28e-02	0.012	137.36	154.90
16045-6-301002	I_J1_6			Infected J1	Early infection	0 (0)	6.54e-05	0	NA	8342.25
16045-8-16110141B01201002	I_J1_8			Infected J1	Early infection	0 (0)	2.65e-02	0.009	149.33	206.28
16045-9-16110141B01301002	I_J1_9			Infected J1	Early infection	0 (0)	3.24e-05	-0.005	NA	3465.50
16045-10-16110141B01401002	I_J1_10			Infected J1	Early infection	0 (0)	7.73e-05	0	NA	5748.03
16045-11-16110141B01501002	I_J1_11			Infected J1	Early infection	0 (0)	2.40e-04	0.001	NA	3267.29
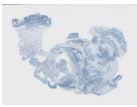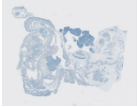
16045-13-601002	I_J1_12			Infected J1	Early infection	2.11 (2.884528e+02)	1.25e-04	0	NA	3166.51
16045-14-16110141B01601002	I_J1_13			Infected J1	Early infection	1.48 (6.209026e+01)	3.78e-03	-0.002	91.80	932.47
64852	I_J1_14			Infected J1	Early infection	0.30 (4.472136e+00)	1.00e-02	-0.006	147.67	250.72
64853	I_J1_15			Infected J1	Early infection	0 (0)	3.96e-04	0	NA	1243.77
16045-16-701002	I_J4_1			Infected J4	Early infection	0.83 (1.520526e+01)	8.32e-02	0.013	182.89	135.35
16045-17-801002	I_J4_2			Infected J4	Early infection	0.96 (1.559487e+01)	4.92e-02	0.011	149.59	265.76

16045-18-901002	I_J4_3			Infected J4	Early infection	0 (0)	1.07e-01	0.019	194.40	89.01
16045-19-1001002	I_J4_4			Infected J4	Early infection	1.25 (4.024922e+01)	2.43e-02	0.008	150.49	172.74
16045-20-1101002	I_J4_5			Infected J4	Early infection	0.34 (4.919350e+00)	1.25e-01	0.022	194.69	89.50
16045-21-1201002	I_J4_6			Infected J4	Early infection	0 (0)	1.56e-02	0.005	111.73	162.54
16045-22-16110141B01701002	I_J4_7			Infected J4	Early infection	0.38 (5.366563e+00)	4.06e-05	0	NA	2789.74
16045-23-16110141B01801002	I_J4_8			Infected J4	Early infection	0 (4.472136e-01)	1.60e-04	0	NA	5256.96

16045-24-16110141B01901002	I_J4_9			Infected J4	Advanced infection	6.93 (4.899656e+06)	5.74	0.267	360.66	52.93
16045-25-1301002	I_J4_10			Infected J4	Advanced infection	7.15 (9.153557e+06)	6.76	0.305	448.62	52.23
16045-28-16110141B02001002	I_J4_11			Infected J4	Advanced infection	7.13 (2.617816e+07)	3.17	0.206	318.66	64.79
16045-29-16110141B02101002	I_J4_12			Infected J4	Advanced infection	6.92 (1.144631e+07)	1.86	0.143	281.03	62.83
16045-31-16110141B02201002	I_J4_13			Infected J4	Advanced infection	6.39 (2.441083e+06)	1.29	0.157	435.73	54.39
16045-32-1701002	I_J4_14			Infected J4	Advanced	6.01 (1.271	8.36	0.322	475.14	46.81

					infecti on	880e+ 06)				
64854	I_J4_ 15			Infec ted J4	Advan ced infecti on	7.12 (1.154 655e+ 07)	2.17	0.163	364.2 0	60.30
64856	I_J4_ 16			Infec ted J4	Advan ced infecti on	7.09 (8.058 702e+ 06)	5.31e- 01	0.074	293.6 1	63.33
64857	I_J4_ 17			Infec ted J4	Advan ced infecti on	6.38 (4.098 913e+ 06)	8.77	0.356	548.6 9	47.50
16049-2- 3101002	C_J1 _1			Cont rol J1	Contr ol	0 (0)	1.01e- 02	0.002	96.65	570.5 0
16049-3- 3201002	C_J1 _2			Cont rol J1	Contr ol	0 (0)	5.76e- 02	0.011	169.9 4	123.9 7
16049-5- 16110141B00 201002	C_J1 _3			Cont rol J1	Contr ol	0 (0)	9.10e- 04	0	NA	8862. 10

40

16049-6-3301002	C_J4_1			Control J4	Control	0 (0)	1.11e-01	0.016	155.01	82.49
16049-7-16110141B00301002	C_J4_2			Control J4	Control	0 (0)	2.77e-02	0.006	134.66	243.27
16049-8-3401002	C_J4_3			Control J4	Control	0 (0)	1.07e-01	0.021	198.75	92.49
16049-10-16110141B00401002	C_J4_4			Control J4	Control	0 (0)	1.17e-02	0	96.75	712.53

684